

1 **Improved parameterization of snow albedo in Noah coupled with WRF:**

2 **Applicability to snow estimates for the Tibetan Plateau**

3 **Lian Liu^{1,2}, Yaoming Ma^{1,2,3,4}, Massimo Menenti^{5,6}, Rongmingzhu Su^{1,2,4}, Nan**
4 **Yao^{1,2,4}, Weiqiang Ma^{1,2,3,4}**

5 [1] {Key Laboratory of Tibetan Environment Changes and Land Surface Processes,
6 Institute of Tibetan Plateau Research, Chinese Academy of Sciences, Beijing, 100101,
7 China}

8 [2] {Land-Atmosphere Interaction and its Climatic Effects Group, State Key
9 Laboratory of Tibetan Plateau Earth System, Resources and Environment (TPESRE),
10 Institute of Tibetan Plateau Research, Chinese Academy of Sciences, Beijing, 100101,
11 China}

12 [3] {CAS Center for Excellence in Tibetan Plateau Earth Sciences, Beijing, 100101,
13 China}

14 [4] {University of Chinese Academy of Sciences, Beijing 100049, China}

15 [5] {State Key Laboratory of Remote Sensing Science, Institute of Remote Sensing and
16 Digital Earth, Chinese Academy of Sciences, Beijing, 100101, China}

17 [6] {Delft University of Technology, Delft, Netherlands}

18 Correspondence to: Y. M. Ma (ymma@itpcas.ac.cn)

19

20 **Abstract**

21 Snow albedo is important to the land surface energy balance and to the water cycle.
22 During snowfall and subsequent snowmelt, snow albedo is usually parameterized as
23 functions of snow related variables in land surface models. However, the default snow
24 albedo scheme in the widely used Noah land surface model shows evident shortcomings
25 in land-atmosphere interactions estimates during snow events on the Tibetan Plateau.
26 Here, we demonstrate that our improved snow albedo scheme performs well after
27 including snow depth as an additional factor. By coupling the WRF and Noah models,
28 this study comprehensively evaluates the performance of the improved snow albedo
29 scheme in simulating eight snow events on the Tibetan Plateau. The modeling results
30 are compared with WRF run with the default Noah scheme and in situ observations.
31 The improved snow albedo scheme significantly outperforms the default Noah scheme
32 in relation to air temperature, albedo and sensible heat flux estimates, by alleviating
33 cold bias estimates, albedo overestimates and sensible heat flux underestimates,
34 respectively. This in turn contributes to more accurate reproductions of snow event
35 evolution. The averaged RMSE relative reductions (and relative increase in correlation
36 coefficients) for air temperature, albedo, sensible heat flux and snow depth reach 27 %
37 (5 %), 32 % (69 %), 13 % (17 %) and 21 % (108 %) respectively. These results
38 demonstrate the strong potential of our improved snow albedo parameterization scheme
39 for snow event simulations on the Tibetan Plateau. Our study provides a theoretical
40 reference for researchers committed to further improving the snow albedo
41 parameterization scheme.

42 **Keywords:** WRF; snow albedo parameterization; turbulent heat and vapor fluxes;
43 Tibetan Plateau

44

45 **1 Introduction**

46 The surface albedo directly determines the proportion of incident solar radiation that is
47 absorbed by the surface, and is an important parameter in climate and land surface
48 models (LSMs) (Sellers et al., 1996). Small changes in surface albedo can affect the
49 energy balance in the land-atmosphere system, and can drive both local and global
50 climate change (Bloch, 1964).

51 Surface albedo changes dramatically during snowfall and snowmelt cycles. Much
52 research has been carried out to identify the factors that influence these changes,
53 including the effects of terrain shielding, altitude, sky conditions, vegetation, and snow
54 properties such as grain size, liquid water content, depth, and impurities (Warren and
55 Wiscombe, 1980; Wiscombe and Warren, 1980; Aoki et al., 2003; Jonsell et al., 2003;
56 Hansen and Nazarenko, 2004; Liang et al., 2005; Wang et al., 2015; He et al., 2018a).
57 This body of research has led to the development of many parameterization schemes
58 for surface albedo (Oerlemans and Knap, 1998; Wang et al., 2007; Bao et al., 2008; Li
59 and Hu, 2009; Gardner and Sharp, 2010; Kuipers Munneke et al., 2011; Malik et al.,
60 2014; Dang et al., 2015; He et al., 2017, 2018b; Meng and Li, 2019; Saito et al., 2019;
61 Wang et al., 2020). Most snow albedo parameterization schemes depend on statistical
62 empirical formulas and constant parameters, rather than representing physical snow-
63 albedo feedback processes. To improve the performance of snow albedo
64 parameterization schemes for simulating land-atmosphere interactions, Bao and Lyu
65 (2009) added consideration of solar zenith angle to a regional climate model, which
66 resulted in a 1.2 °C temperature increase, and considerably improved the cold bias in
67 East Asia and improved the representation of diurnal ground temperature changes in
68 northwest China. Park and Park (2016) investigated the effect of vegetation on snow
69 covered surface albedo and improved the winter surface albedo estimates from their
70 LSM by including leaf and stem indices in the snow albedo parameterization scheme,
71 which reduced the root mean square error (RMSE) by 69 %. Zhong et al. (2017)
72 considered aerosol radiative effects on snow processes in their simulations and

73 successfully reproduced the snow albedo and snow depth. Fresh snow albedo depends
74 on snow depth, and albedo parameterization schemes that fail to account for this
75 generally overestimate the snow depth. To address this, Wang et al. (2020) developed a
76 new albedo scheme for fresh snow, which accounts for the relationship between fresh
77 snow albedo, snow grain size and snow depth, resulting in improved snow depth
78 estimates during the snow ablation period on the Tibetan Plateau. This highlights the
79 importance of accounting for the effect of snow depth on fresh snow albedo.

80 A coupled land-atmosphere model can provide useful insights into conditions on the
81 Tibetan Plateau, where the terrain is complex and there are few, and unevenly
82 distributed observation stations (Maussion et al., 2011; Yuan et al., 2016; Norris et al.,
83 2017; Bonekamp et al., 2018; Rahimi et al., 2019). However, the parameterization
84 scheme for surface albedo in the Noah LSM, which is currently the most widely used
85 LSM, does not account for all the factors that influence albedo. It includes many
86 predetermined parameters and an approximate treatment of vegetation, soil and snow,
87 which can result in some inaccuracies in the estimated surface albedo (Wen et al., 2011;
88 Liu et al., 2019). For example, the surface albedo parameterization scheme in the Noah
89 LSM considers snow cover and age, but ignores other snow related factors, such as
90 snow depth, that can drive dramatic changes in albedo (Ek et al., 2003). This makes it
91 inappropriate to use the Noah LSM to characterize changes in snow albedo that follow
92 from snowfall and melt processes in complex topographic areas. However, the Noah
93 LSM appears to be the most readily available snow albedo scheme for long term climate
94 modeling research (Rai et al., 2019). Despite its shortcomings, the Noah albedo
95 parameterization scheme does provide substantial improvements to estimates of the
96 magnitude and timing of both the peak snowfall amount and the maximum snow cover
97 extent, following from the scheme's consideration of snow albedo decay and liquid
98 water refreezing (Livneh et al., 2010). The above issues represent opportunities for
99 improvements to be made to the snow albedo parameterization scheme in the Noah
100 LSM.

101 The use of an advanced snow albedo parameterization scheme is crucial for accurate
102 estimation of land-atmosphere interactions over the Tibetan Plateau, where the snow-
103 albedo effect is extremely strong. It has been shown that the Weather Research and
104 Forecasting (WRF; Skamarock et al., 2008) model, when coupled with the default Noah
105 albedo parameterization scheme, results in an apparent cold bias over the Tibetan
106 Plateau (Gao et al., 2015; Meng et al., 2018; Liu et al., 2019). This bias can be reduced
107 by including albedo products from the Moderate Resolution Imaging
108 Spectroradiometer (MODIS) and an additional snow depth parameter as independent
109 variables in the Noah albedo parameterization scheme (Liu, 2020). This approach is not
110 the same as assimilating satellite retrieved snow related products into the LSM, which
111 has also been shown to lead to improvements (Xu and Shu, 2014; Zhang et al., 2014;
112 Lin et al., 2016; Xue et al., 2019). This improved snow albedo scheme has been
113 successfully implemented in the WRF model, coupled with Noah, to simulate land-
114 atmosphere interactions during a regional heavy snow event on the Tibetan Plateau (Liu,
115 2020). However, it has not been shown that the improvements that follow from the
116 improved snow albedo scheme are universal over the Tibetan Plateau, and this should
117 be studied further. Severe snowfall occurs often over the southern Tibetan Plateau,
118 while snowfall over the eastern Tibetan Plateau is generally of relatively weak intensity,
119 and the rate of snowmelt varies widely depending on the heterogeneous underlying
120 surfaces. This makes it necessary to carry out numerical experiments that focus on snow
121 events over the eastern and southern Tibetan Plateau to assess how reliably the
122 improved scheme can be used to characterize different snowfall intensities and
123 snowmelt processes.

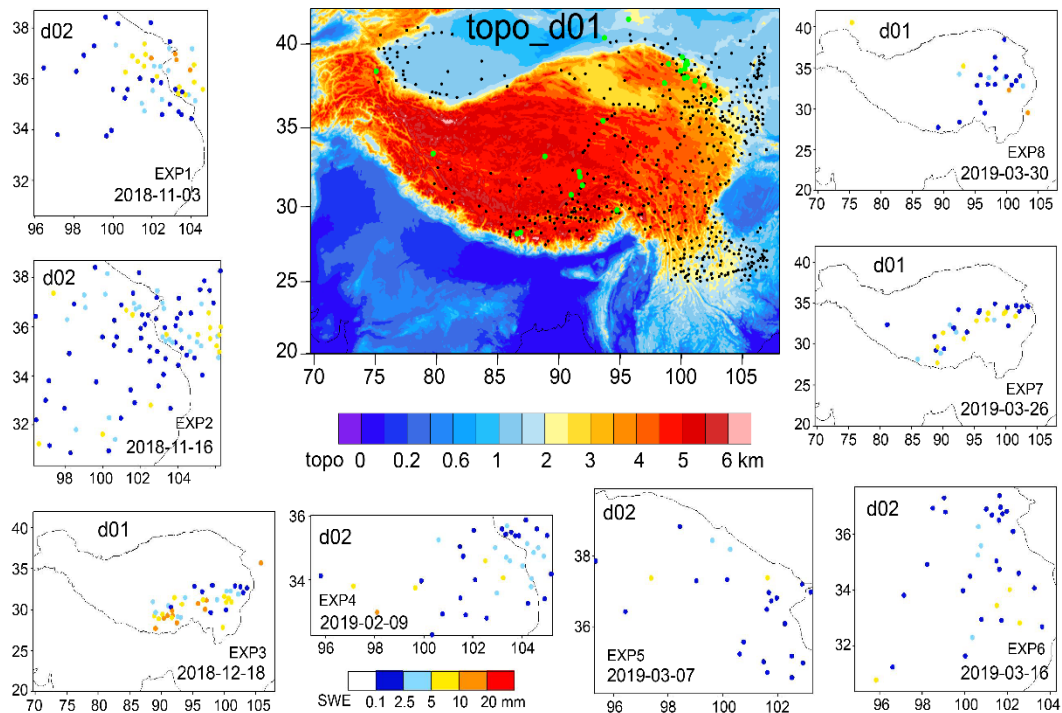
124 In this study, we selected eight moderate to snowstorm events that occurred over the
125 southern and eastern Tibetan Plateau to assess the universality of the improvements
126 offered by our improved snow albedo scheme in WRF coupled with the Noah LSM.
127 For each snow event, two numerical experiments were carried out: one implementing
128 the default Noah snow albedo scheme, and the other implementing our improved snow
129 albedo scheme. The model performance was assessed through comparison of the

130 modeled air temperature, albedo, snow depth, turbulent heat and vapor fluxes with
131 ground observations. The aim of this study is to explore the potential of our improved
132 snow albedo parameterization scheme to simulate snow events over the whole Tibetan
133 Plateau more accurately than can be done using the standard default scheme. We hope
134 that this study will also provide a useful reference for researchers working to develop
135 and improve this, and other albedo parameterization schemes.

136 **2 Data and methodology**

137 **2.1 Description of snow events**

138 We selected China Meteorological Administration (CMA) national observation stations
139 on the Tibetan Plateau, and in the surrounding regions, with elevations exceeding 1000
140 m. This resulted in a total of 502 stations (Figure 1 shows their distribution). Snowfall
141 events were identified from the hourly air temperature and precipitation observations
142 from all 502 stations when the air temperature was below 0 °C. Daily snowfall amounts
143 were calculated, using 08:00 Beijing Standard Time (BST) as the start and end time for
144 each day. The standards to define snowfall grade were taken from the China
145 Meteorological Standardization Network (<http://www.cmastd.cn/>). Using these
146 standards, eight different grades of snowfall event were considered in our study,
147 including moderate, heavy and snowstorm. Most of the snowfall events took place over
148 the eastern Tibetan Plateau, and some occurred in a large region across the southern and
149 central to the eastern Tibetan Plateau. The maximum daily snowfall amount from all
150 snowfall events exceeded 8 mm, and four events resulted in more than 10 mm daily
151 snowfall, making these snowstorm grade events. Snow depth is much greater on the
152 southern Tibetan Plateau (> 50 cm) than it is on the eastern and central Tibetan Plateau
153 (<=20 cm). The description of eight snowfall events, including the date and location of
154 moderate to snowstorm grade events, the maximum snow depth and daily snowfall
155 amount, are detailed in Table 1. The daily snowfall amounts from the eight snowfall
156 events are shown in Figure 1.



157

158 **Figure 1.** WRF domains of d01 and d02, and CMA observations of daily snowfall
 159 amount in color solid circles for the eight experiments. The topographical height of d01
 160 is shaded with black solid circles indicating the locations of the CMA stations, and
 161 green solid circles indicating the locations of the CAS stations and the Qilian Mountains
 162 integrated observatory network.

163

164

165

166

167

168

169

170

171 **Table 1** Description of eight snowfall events using China Meteorological
 172 Administration observations.

Snow events	Event 1	Event 2	Event 3	Event 4	Event 5	Event 6	Event 7	Event 8
Date of moderate to snowstorm	Nov. 3-6, 2018	Nov. 15-17, 2018	Dec. 17-18, 2018	Feb. 9, 2019	Mar. 7-8, 2019	Mar. 16, 2019	Mar. 26, 2019	Mar. 30-Apr. 1, 2019
Region in the Tibetan Plateau	eastern	eastern	southern, central, eastern	eastern	eastern	eastern	southern, central, eastern	central, eastern
Maximum daily snowfall amount (unit: mm)	13.6	9.2	18.7	11	9.3	9.1	8.7	14.3
Maximum snow depth (unit: cm)	18	16	65	20	13	9	53	18

173 **2.2 Model description and experiment configuration**

174 The WRF model (Skamarock et al., 2008), version 3.7.1, coupled with the Noah LSM,
 175 was used to simulate the eight snowfall events in this study. It is a fully compressible,
 176 non-hydrostatic model and includes a run time hydrostatic option. Vertical levels are
 177 determined using a mass based terrain following hydrostatic pressure coordinate, and
 178 calculations are performed on an Arakawa C grid. The model uses 2nd and 3rd order
 179 Runge-Kutta time integration schemes, and 2nd to 6th order advection schemes in both
 180 the horizontal and vertical direction.

181 The extremely steep terrain on the central and southern Tibetan Plateau led to model
 182 instability and failure for snowfall events 3, 7 and 8 when a relatively fine horizontal
 183 resolution of 1 km was used; however, the calculations remained stable when the
 184 resolution was increased to 5 km. We therefore used two ways nested modeling domains

185 in our model configuration for snowfall events 1, 2, 4, 5 and 6, and a single modeling
186 domain for snowfall events 3, 7 and 8. The coarse domain (d01) was used to simulate
187 synoptic scale atmospheric conditions over 20.0-42.0° N and 69.7-108.0° E with a
188 horizontal resolution of 5 km. The inner domain (d02) had a horizontal resolution of 1
189 km, and event 1 occupied 876×966 grid cells, event 2 occupied 976×1001 cells, event
190 4 was resolved by 966×451 cells, event 5 was calculated over 781×686 cells, and
191 event 6 covered 926×881 cells. The vertical structure of both domains included 35
192 unevenly spaced layers and extended up to 50 hPa. The model was configured to use
193 the Noah LSM in d01 and d02 to describe all land-atmosphere interactions; the
194 Thompson scheme to represent microphysical processes; the Dudhia scheme to
195 represent shortwave radiation, the RRTM scheme to describe longwave radiation; the
196 YSU scheme to describe the planetary boundary layer; and only in d01 to use the Kain-
197 Fritsch cumulus parameterization scheme for clouds.

198 We conducted numerical experiments to simulate snow event 1 (EXP1), event 2 (EXP2),
199 event 3 (EXP3), event 4 (EXP4), event 5 (EXP5), event 6 (EXP6), event 7 (EXP7) and
200 event 8 (EXP8). The model domains for the experiments are shown in Figure 1. Each
201 experiment included two model simulations: one implementing the default Noah snow
202 albedo parameterization scheme, and the other implementing a new improved snow
203 albedo scheme. The new improved snow albedo was developed based on conversion
204 formula from MODIS narrowband spectral reflectance to broadband albedo following
205 Liang (2000) and albedo calculation formula about fresh snow, firn and bare ground
206 albedo, snow age and depth following Oerlemans and Knap (1998). MODIS broadband
207 albedo and WRF modeled snow depth and age were used to estimate the related
208 parameters i.e., firn albedo and scales of snow depth and age through nonlinear fitting
209 of the above albedo calculation formula. The final nonlinear fitting results produced the
210 new improved snow albedo scheme, seeing the equations (3) and (4). The snow albedo
211 is parameterized using Eq. (1) and (2) in the default Noah land surface scheme (Livneh
212 et al., 2010), and using Eq. (3) and (4) in the improved scheme (Liu, 2020):

213

$$\alpha_{\text{snow}} = \alpha_{\text{max}} \times A^{t^B} \quad (1)$$

$$\alpha = \alpha_{bg} + sc \times (\alpha_{\text{snow}} - \alpha_{bg}) \quad (2)$$

$$\alpha_{\text{snow}} = 0.13 + 0.66e^{\left(\frac{t}{1.38}\right)} \quad (3)$$

$$\alpha = \alpha_{\text{snow}} + (0.19 - \alpha_{\text{snow}})e^{\left(\frac{-d}{0.11}\right)} \quad (4)$$

216 where A and B are constants, equal to 0.94 and 0.58, respectively, for snow
217 accumulation periods, and are 0.82 and 0.46, respectively, for other periods; α_{bg} is the
218 background albedo, which depends on the land cover type; sc is snow cover, and
219 ranges from 0 to 1; α_{max} is fresh snow albedo; α_{snow} is snow albedo; t is the snow
220 age in units of days; d is snow depth in meters.

221 The fifth generation European Centre for Medium Range Weather Forecasts (ECMWF)
222 reanalysis dataset (ERA5), with a spatial resolution of $0.25^\circ \times 0.25^\circ$ and 3 h temporal
223 resolution, provided initial and boundary conditions for our numerical experiments. The
224 ERA data were calculated using 4DVar data assimilation in CY41R2 from ECMWF's
225 Integrated Forecast System, with 137 vertical hybrid sigma/pressure levels, extending
226 to 0.01 hPa. ERA5 is freely available from the website
227 <https://www.ecmwf.int/en/forecasts/datasets/reanalysis-datasets/era5>. The near real
228 time MODIS land cover product was used to replace the outdated land cover in WRF
229 preprocessing system. We ran the model from before the onset of each snowfall event
230 until and after all snowmelt following the event had ceased. EXP1 was run Nov. 1-8
231 2018, EXP2 was run Nov. 13-18 2018, EXP3 was run Dec. 16-20 2018, EXP4 was run
232 Feb. 5-11 2019, EXP5 was run Mar. 2-10 2019, EXP6 was run Mar. 12-18 2019, EXP7
233 was run Mar. 24-29 2019, EXP8 was run Mar. 28-Apr.7 2019. The model results were
234 output at 3 hours intervals and the first day was used for model spin up.

235 **2.3 Data for model evaluation and comparison**

236 CMA hourly observations of air temperature and snow depth from 502 stations were

237 used to assess the WRF model estimates of 2 m air temperature and snow depth that
238 were made using the improved snow albedo parameterization scheme. Albedo is a key
239 factor for net radiation calculations, and is defined as the ratio of reflected shortwave
240 radiation (upwards) to received shortwave radiation (downwards). It determines the
241 distribution of turbulent land surface heat fluxes between sensible (SH) and latent heat
242 (LH). There are many meteorological observations available that have been
243 continuously recorded on the Tibetan Plateau at atmospheric boundary layer towers,
244 eddy covariance systems (Ma et al., 2018, 2020) and the Qilian Mountains integrated
245 observatory network (Li, 2019; Liu et al., 2020; Zhao and Zhang, 2020). These provide
246 in situ data that are assumed to constitute ‘truth’ for the model validation in this study.
247 In situ observations of albedo, SH and LH from 11 Chinese Academy of Sciences (CAS)
248 stations/samples, and from 16 stations in the Qilian Mountains integrated observatory
249 network are used to evaluate the accuracy of the improved snow albedo
250 parameterization scheme for modeling snow events on the Tibetan Plateau. It is
251 reasonable to compare observations of albedo, SH and LH with model estimates at 5
252 km resolution because there are only a few in situ observation stations in d02, but a
253 total of 27 observation stations in d01. At local solar noon in Lhasa (14:00 BST), the
254 observed albedo value is closer to the Lambertian albedo that is described by the WRF
255 model when coupled with LSMs. We therefore used albedo observations made at 14:00
256 BST to evaluate the model calculated albedo. Quality control codes 1, 2 and 3 were
257 selected when using the Turbulence Knight version 3 (TK3) software, and 0 was used
258 when using the Eddypro software to calculate SH and LH. Details of the 27 stations
259 from the CAS and the Qilian Mountains integrated observatory network that were used
260 in our study are provided in Table 2, and their locations on the Tibetan Plateau are
261 shown in Figure 1. In order to compare WRF simulations against in situ observations,
262 sampling the gridded model estimates and interpolating to given ground stations’
263 locations were done by bi-linear interpolation of the four surrounding model grid points.
264 The RMSE and the correlation coefficient were calculated for the assessment of the
265 model performance in relation to albedo, air temperature, SH, LH, and snow depth

266 estimates.

267 **Table 2** Location of stations from the Chinese Academy of Sciences (CAS) and the
268 Qilian Mountains integrated observatory network, and whether or not observations of
269 albedo, SH and LH were used from each station.

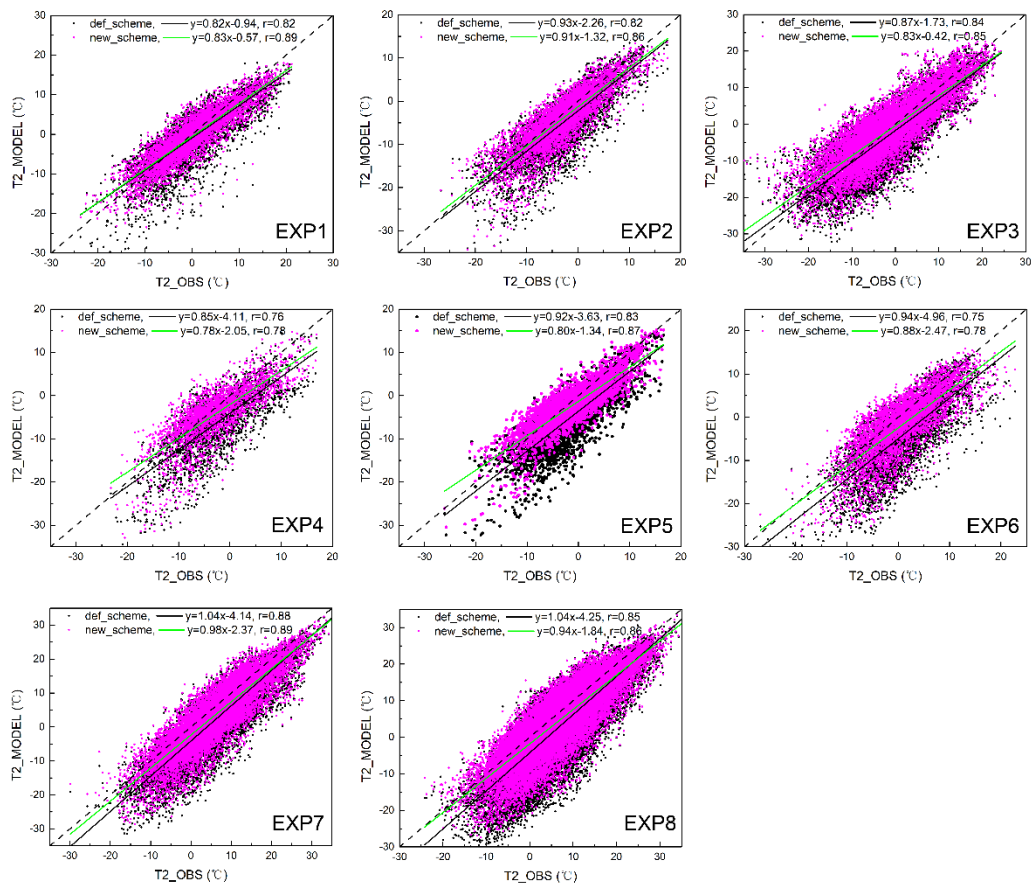
Station No.	Station Name	Station Type	Latitude (° N)	Longitude (° E)	Elevation (m)	Using albedo	Using SH and LH
1	SETS	CAS	29.77	94.73	3326	Yes	No
2	QOMS	CAS	28.21	86.56	4276	Yes	Yes
3	QOMS sample	CAS	28.31	86.85	4600	No	Yes
4	MASWE	CAS	38.41	75.05	3668	Yes	No
5	Nam Co	CAS	30.77	90.99	4730	Yes	Yes
6	NASDE	CAS	33.39	79.70	4264	Yes	No
7	Shuanghu	CAS	33.22	88.83	4947	Yes	Yes
8	NewD66	CAS	35.43	93.59	4465	Yes	No
9	BJ	CAS	31.37	91.90	4509	Yes	Yes
10	MS3478	CAS	31.93	91.71	4620	Yes	No
11	Amdo	CAS	32.24	91.62	4695	Yes	No
12	Yakou	Qilian	38.01	100.24	4148	Yes	Yes
13	Arou	Qilian	38.05	100.46	3033	Yes	Yes
14	Jingyangling	Qilian	37.84	101.12	3750	Yes	Yes
15	Dashalong	Qilian	38.84	98.94	3739	Yes	Yes
16	Heihe Remote Sensing	Qilian	38.83	100.48	1560	Yes	No
17	Huazhaizi Desert Steppe	Qilian	38.77	100.32	1731	Yes	Yes
18	Daman	Qilian	38.86	100.37	1556	Yes	Yes
19	Zhangye wetland	Qilian	38.96	100.45	1460	Yes	Yes
20	Guazhou	Qilian	41.41	95.67	2014	Yes	Yes
21	Dayekou	Qilian	38.56	100.29	2703	Yes	No
22	Dunhuang	Qilian	40.35	93.71	993	Yes	No
23	Liancheng	Qilian	36.69	102.74	2903	Yes	No
24	Linze	Qilian	39.24	100.06	1402	Yes	No
25	Sidalong	Qilian	38.43	99.93	3146	Yes	No
26	Xiyinghe	Qilian	37.56	101.86	3616	Yes	No

27	Tianjun	Qilian	37.70	98.61	3718	Yes	Yes
----	---------	--------	-------	-------	------	-----	-----

270 **3 Results**

271 **3.1 Air temperature**

272 Albedo is a key factor in determining the net radiation received at the surface, which
273 determines the land surface energy balance and influences air temperature. Scatterplots
274 of the air temperatures estimated by the WRF model and observed at the CMA stations
275 are shown in Figure 2. In all eight modeling experiments, implementing the improved
276 snow albedo scheme in the WRF model greatly reduces the cold bias that occurs when
277 the default Noah snow albedo scheme is used. Where the default Noah scheme results
278 in a warm bias at the observed lower air temperature for EXP1 and EXP3, however, the
279 improved albedo scheme does not improve the accuracy of the WRF estimates.
280 Compared with cold bias caused by the default Noah albedo scheme at the observed
281 lower air temperature, the improved snow albedo scheme results in a warm bias for
282 EXP2, EXP4 and EXP5. On the whole, scatterplots comparing air temperature
283 observations from CMA station with WRF estimates made using the improved snow
284 albedo scheme estimates, show the data to be concentrated near the ideal fitting line,
285 where the model has exactly reproduced the observations. Using the improved snow
286 albedo scheme results in a marked reduction in the cold bias for the WRF model
287 estimates for EXP1, EXP2, EXP4, EXP5 and EXP6, and the greatest reduction in the
288 cold bias, for all eight experiments, occurs for EXP6 (Fig. 2).



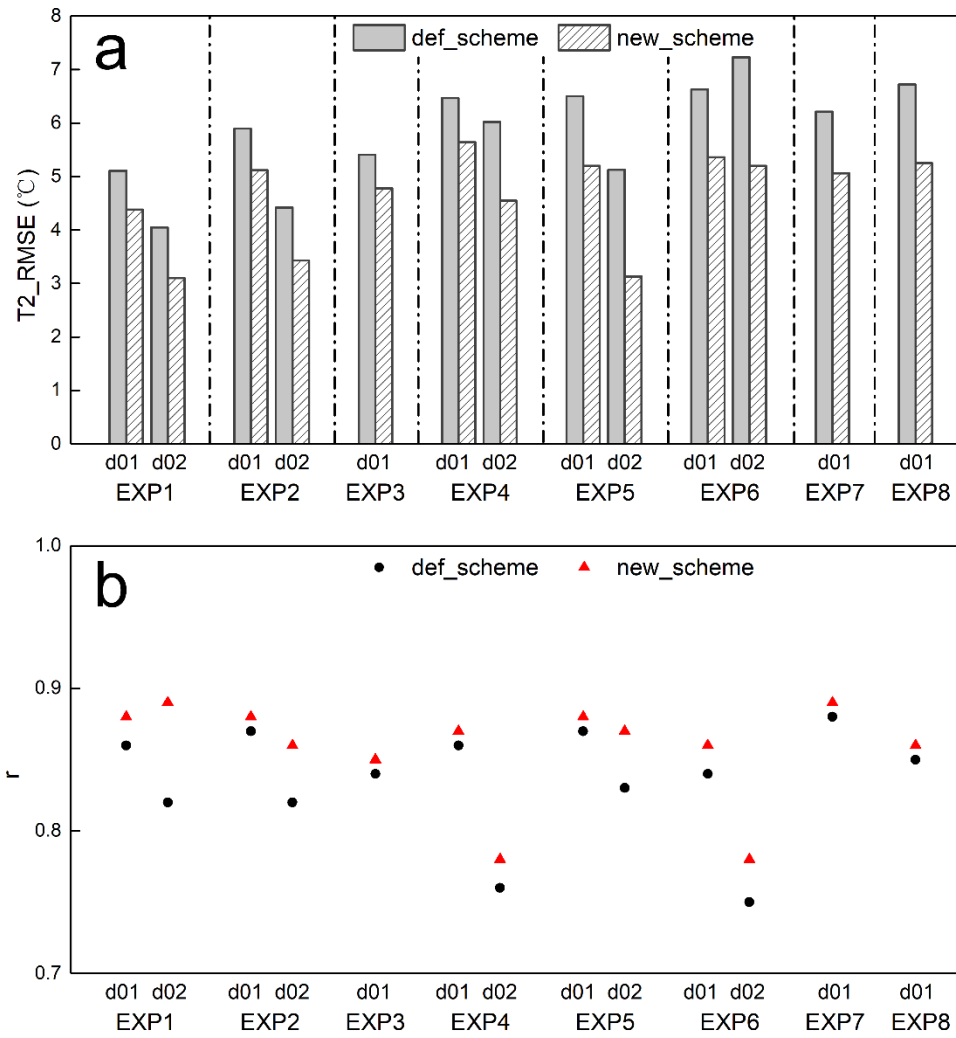
289

290 **Figure 2.** Scatterplot of air temperature, comparing the CMA observations and model
 291 estimates for the eight experiments in the inner (high resolution) model domain from
 292 WRF, using the default Noah snow albedo scheme (def_scheme, black solid circle), and
 293 using the improved snow albedo scheme (new_scheme, red solid circle). The black
 294 solid line is a linear fit to the black solid circles. The green solid line is a linear fit to
 295 the red solid circles. The black dotted line is the line $y=x$. r is the correlation coefficient
 296 between the CMA observations and the model estimates. The correlation coefficient (r)
 297 is significant at 0.01 significance level.

298 To quantify the improvement to air temperature estimates that follows from
 299 implementation of the improved snow albedo scheme, the RMSE and correlation
 300 coefficient was calculated between CMA observations and model estimates of air
 301 temperature, shown in Figure 3. The differences between the accuracy of the new
 302 scheme and the default scheme are shown in Table 3. The accuracy of WRF air

303 temperature estimates varies between the different snowfall events, between the
304 different snow albedo schemes, and also varies with model resolution. The lowest air
305 temperature RMSE and the highest correlation coefficient are 3.1 °C and 0.89,
306 respectively, and both occur for EXP1. The highest air temperature RMSE and the
307 lowest correlation coefficient occur for EXP6, reaching 7.2 °C and 0.75, respectively.
308 Air temperature RMSE generally ranges from 4.1 to 7.2 °C for the WRF estimates that
309 were made using the default Noah snow albedo scheme estimates, with correlation
310 coefficients ranging from 0.75 to 0.88. In contrast, when the improved snow albedo
311 scheme is implemented in WRF, the RMSE ranges from 3.1 to 5.6 °C, and the
312 correlation coefficients range from 0.78 to 0.89. Compared with when the default Noah
313 snow albedo scheme is used, the maximum decrease in air temperature RMSE when
314 the new scheme is used reaches 2.03 °C, which represents an improvement of 28.1 %,
315 and the average decrease in air temperature RMSE is 1.2 °C, representing an
316 improvement of 20.7 %. There is an improvement of more than 11 % in the RMSE for
317 all eight experiments with the maximum improvement of 39 % when the new albedo
318 scheme is used, relative to when the default scheme is used. Implementing the improved
319 snow albedo scheme in WRF for all eight experiments also increased the correlation
320 coefficient between observed and modeled air temperature, by 0.01-0.07, which
321 represents an improvement of 1-9 % (Fig. 3, Table 3).

322 Compared with using the default Noah snow albedo scheme, using the improved
323 scheme results in improved model estimates for all eight EXPs, decreasing the air
324 temperature RMSE and increasing the correlation coefficient when compared with
325 observations. These improvements occur for air temperature estimates calculated at
326 both 5 km and 1 km resolution. The improvement to WRF model estimates is greater
327 for calculations made at 1 km resolution than at 5 km resolution, and air temperature
328 estimates are more accurate at 1 km resolution than at 5 km resolution by implementing
329 the improved albedo scheme (Fig. 3, Table 3). Therefore, fine resolution (i.e., 1 km) is
330 strongly recommended for future snowfall event modeling studies.



331

332 **Figure 3.** RMSE (a) and correlation coefficient (b) for air temperature (T2) between
 333 observations and model estimates in d01 and d02. The correlation coefficient is
 334 significant at the 0.01 significance level. For def_scheme and new_scheme, see Figure
 335 2.

336

337

338

339

340 **Table 3** RMSE and correlation coefficient (r) for air temperature between CMA
341 observations and model estimates, calculated using the default Noah snow albedo
342 scheme (def_scheme) and the improved albedo scheme (new_scheme). The difference
343 in RMSE is new_scheme RMSE minus def_scheme RMSE. The difference in r is
344 new_scheme r minus def_scheme r. P value <0.05 is the significance test for the
345 correlation.

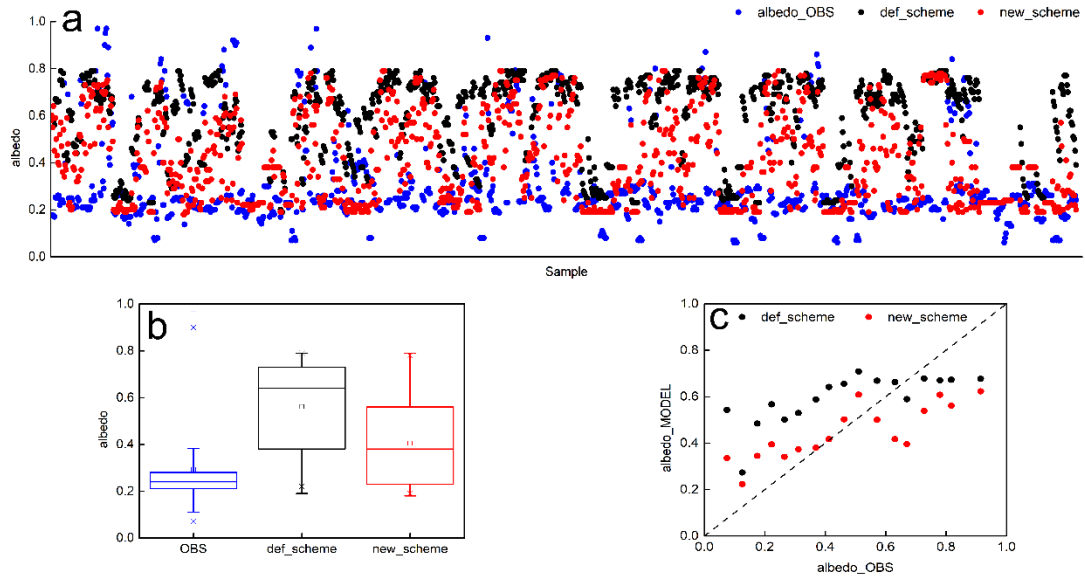
EXPs	Model Domain	RMSE (°C)				r			
		def_ scheme	new_ scheme	Difference	Relative Difference	def_ scheme	new_ scheme	Difference	Relative Difference
EXP1	d01	5.11	4.38	-0.73	-14.3 %	0.86	0.88	0.02	2.3 %
	d02	4.05	3.1	-0.95	-23.5 %	0.82	0.89	0.07	8.5 %
EXP2	d01	5.9	5.12	-0.78	-13.2 %	0.87	0.88	0.01	1.1 %
	d02	4.42	3.43	-0.99	-22.4 %	0.82	0.86	0.04	4.9 %
EXP3	d01	5.41	4.78	-0.63	-11.6 %	0.84	0.85	0.01	1.2 %
EXP4	d01	6.47	5.64	-0.83	-12.8 %	0.86	0.87	0.01	1.2 %
	d02	6.02	4.55	-1.47	-24.4 %	0.76	0.78	0.02	2.6 %
EXP5	d01	6.5	5.2	-1.30	-20.0 %	0.87	0.88	0.01	1.1 %
	d02	5.13	3.13	-2.00	-39.0 %	0.83	0.87	0.04	4.8 %
EXP6	d01	6.63	5.36	-1.27	-19.2 %	0.84	0.86	0.02	2.4 %
	d02	7.23	5.2	-2.03	-28.1 %	0.75	0.78	0.03	4.0 %
EXP7	d01	6.21	5.06	-1.15	-18.5 %	0.88	0.89	0.01	1.1 %
EXP8	d01	6.72	5.25	-1.47	-21.9 %	0.85	0.86	0.01	1.2 %

346 **3.2 Albedo**

347 Using the improved albedo scheme in the WRF model greatly reduces the cold air
348 temperature bias that otherwise occurs, indicating an improvement to model
349 performance. It is necessary to compare albedo estimates with in situ observations.
350 There are very few observation stations located in the finer model domain, and so a
351 total of 26 stations in d01 were used to evaluate the performance of the WRF

352 simulations of albedo at 5 km resolution (Table 2).

353 Scatterplots comparing observations and WRF estimates for albedo in the eight
354 experiments, when both the default and improved snow albedo scheme were used, are
355 shown alongside our statistical analysis in Figure 4. Albedo higher than 0.7 is
356 interpreted as snowfall. Albedo in the range of 0.4 to 0.6 is interpreted as snowmelt.
357 Albedo lower than 0.3 indicates sparse or patchy snow cover at the in situ stations. For
358 all eight snowfall events, the observed albedo is concentrated at low values, with a
359 median of 0.24, while WRF estimated albedo using the default Noah snow albedo
360 scheme has higher values, with a median of 0.64. Compared with albedo estimates
361 calculated using the default scheme, WRF estimates made using the improved scheme
362 result in a prolonged snowmelt period, which increases the number of snowmelt
363 samples and leads to a median albedo of 0.38, which is closer to that for the in situ
364 observations. The mean albedo estimated from WRF using the improved scheme is 0.4,
365 which is also closer to the observed mean of 0.3, than the mean of 0.6 calculated from
366 WRF using the default scheme (Fig. 4a, 4b). In general, the accuracy of the WRF
367 estimates when the new scheme is used is closely related to the observed albedo.
368 Compared with the WRF estimates made using the default Noah scheme, the WRF
369 estimates made using the improved scheme greatly reduce the overestimation of albedo
370 when the observed values are below 0.6, but seem to increase the underestimation of
371 albedo when the observed values are higher than 0.6 (Fig. 4c).

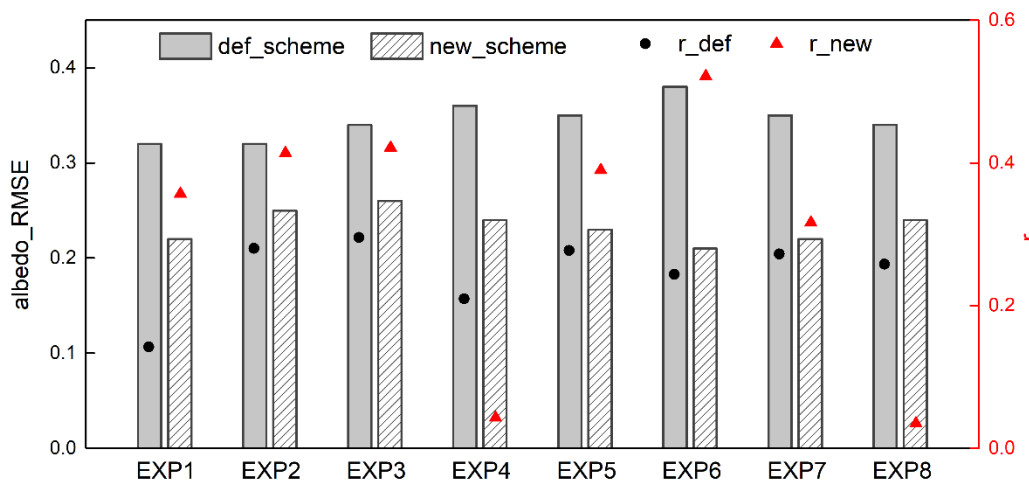


372

373 **Figure 4.** Scatterplot of albedo from observations and model estimates for the eight
 374 experiments (a: horizontal axis denotes samples from EXP1 to EXP8), corresponding
 375 box-and-whisker plot (b) with lower and upper boundaries of the box indicating the
 376 first and third quartiles of albedo respectively and the line inside the box indicating the
 377 median of albedo, and averaged albedo observations every 0.05 segments (i.e., 0-0.049,
 378 0.05-0.099, 0.1-0.149, 0.15-0.199,....., 0.85-0.899, 0.9-0.949, 0.95-0.999) and model
 379 estimates at the same time as observations for all experiments (c). For def_scheme and
 380 new_scheme, see Figure 2.

381 To further evaluate the accuracy of WRF albedo estimates when the different snow
 382 albedo schemes are used, we calculated the RMSE and correlation coefficients between
 383 the observations and the model estimates (Figure 5). The RMSE for the WRF estimates,
 384 when compared to the observations, ranges from 0.32 to 0.38 for the eight experiments
 385 when the default scheme is used, and ranges from 0.21 to 0.26 when the improved
 386 scheme is used. Compared with the default Noah snow albedo scheme, the improved
 387 scheme results in a 0.1 decrease to the albedo RMSE in EXP1, representing a relative
 388 decrease of 31.3 %; a 0.07 decrease in EXP2, representing a relative decrease of 21.9 %;
 389 a 0.08 decrease in EXP3, representing a relative 23.5 % decrease; a 0.12 decrease in
 390 EXP4 and EXP5, representing relative decreases of 33.3 % and 34.3 %, respectively;

391 0.17 decrease in EXP6, representing a relative 44.7 % decrease; a 0.13 decrease in
 392 EXP7, representing a relative 37.1 % decrease; and a 0.1 decrease in EXP8,
 393 representing a relative 29.4 % decrease. With the exceptions of EXP4 and EXP8,
 394 correlations between the modeled and observed albedo are significant at the 0.01
 395 significance level. Implementing the improved albedo scheme in WRF increases the
 396 albedo correlation coefficient by 0.21 in EXP1, a relative increase of 151 %; by 0.13 in
 397 EXP2, a relative increase of 47.6 %; by 0.13 in EXP3, a relative increase of 42.5 %; by
 398 0.11 in EXP5, a relative increase of 40.7 %; by 0.28 in EXP6, a relative increase of
 399 114 %; and by 0.04 in EXP7, a relative increase of 16.2 % (Fig. 5). In general, during
 400 snowfall and the snowmelt period that follows it, implementing WRF using the
 401 improved snow albedo scheme outperforms implementing WRF using the default Noah
 402 scheme and results in more accurate albedo estimates, demonstrated by considerable
 403 decreases in RMSE and increases in the correlation coefficients.

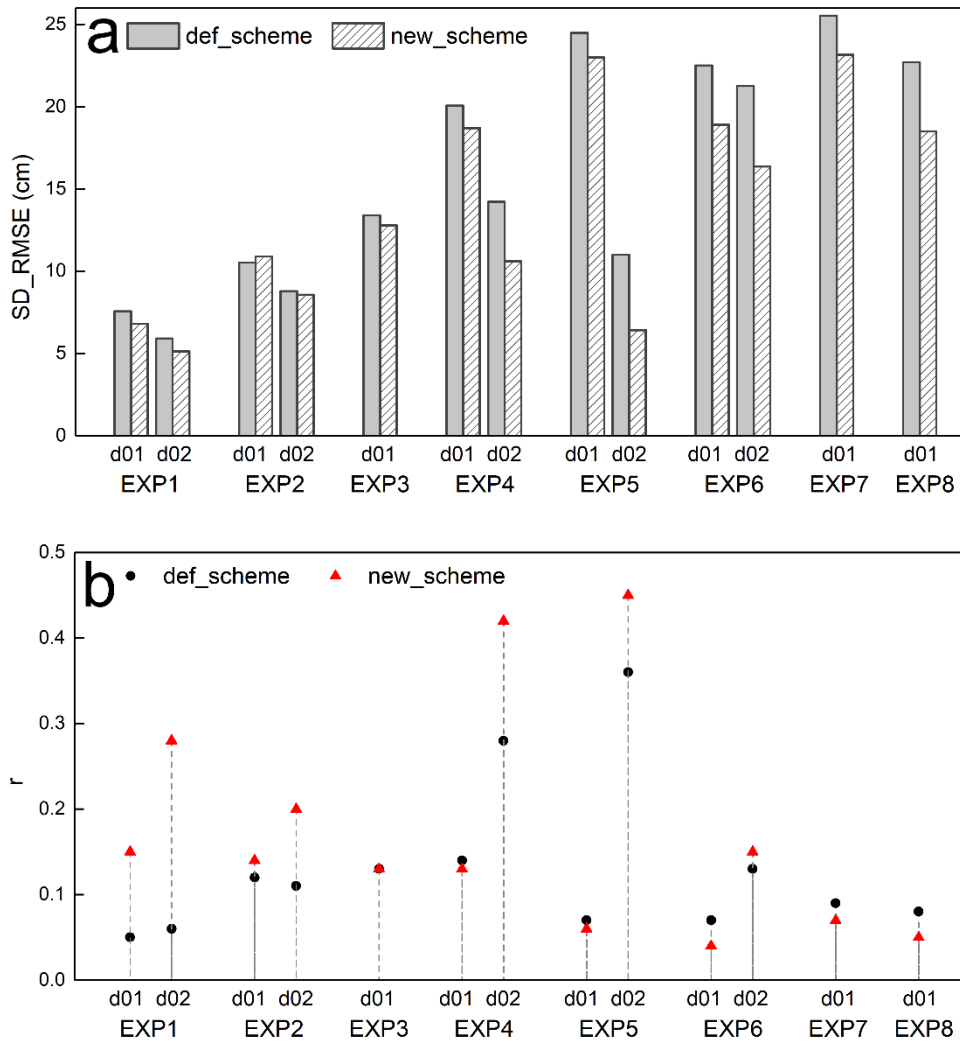


404

405 **Figure 5.** RMSE in column and correlation coefficient (r) in scatterplot for albedo,
 406 comparing observations and model estimates. r_def and r_new mean r between the
 407 observations and WRF-estimates using the default albedo scheme, and using the
 408 improved albedo scheme, respectively. Except EXP4 and EXP8, the correlation
 409 coefficient is significant at the 0.01 significance level. For def_scheme and
 410 new_scheme, see Figure 2.

411 **3.3 Snow depth**

412 There is a feedback between albedo and snow. Snow accumulation and snowmelt
413 influence the proportion of solar irradiance that is reflected; albedo indirectly and non-
414 negligibly influences snow accumulation and snowmelt by affecting the land surface
415 energy budget. In this study, we use an improved snow albedo scheme in which albedo
416 is parameterized as a function of snow depth and age. WRF model estimates of albedo
417 calculated using the improved snow albedo scheme outperform those calculated using
418 the default Noah scheme when snowfall events are simulated, and this leads to
419 improved representation of snowfall and the subsequent snowmelt processes in WRF
420 when the improved scheme is used. Instantaneous direct measurements of snow depth
421 are recorded during snowfall events and over the subsequent snowmelt period. We use
422 these to quantify the improvement that using the new albedo scheme makes to snow
423 estimates calculated in WRF. We assess this by calculating the RMSE and correlation
424 coefficient between the model snow depth estimates and CMA observations, as shown
425 in Figure 6.



426

427 **Figure 6.** Same as Figure 3, but for RMSE (a) and correlation coefficient (b) for snow
 428 depth (SD). The correlation coefficient is significant at the 0.01 significance level,
 429 except for d01 estimates in EXP6.

430 Comparing the accuracy of WRF snow depth estimates calculated using the new
 431 scheme, to the accuracy achieved using the default Noah scheme, the greatest relative
 432 decrease in RMSE is 41.7 %, which occurs for estimates made at finer resolution in
 433 EXP5. Replacing the default albedo scheme with the new scheme in WRF results in an
 434 average decrease in snow depth RMSE of 2.2 cm, which is a 13.4 % improvement. In
 435 areas covered by the higher resolution model domain, the average RMSE decrease is
 436 2.8 cm, which is a 21.2 % improvement. This shows that the impact of replacing the

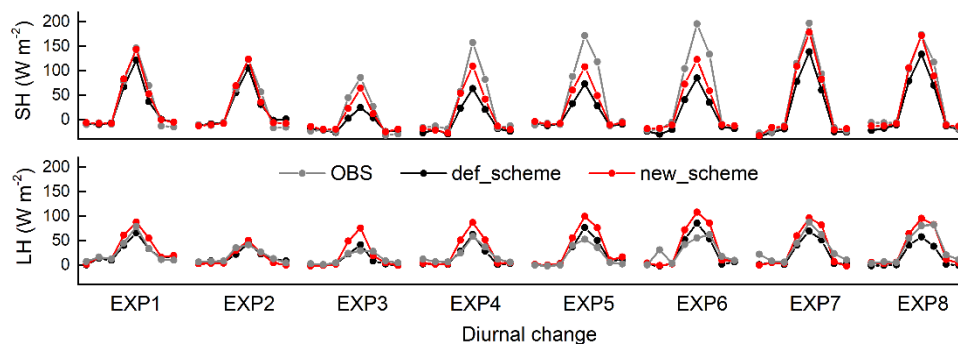
437 albedo scheme with an improved scheme is more significant for areas in the higher
438 resolution d02 model domain than for areas in the coarser d01 model domain (Fig. 6a).
439 Using the improved albedo scheme in WRF increases the correlation coefficient
440 between observed and modeled snow depth in areas within the d02 model domain, but
441 this increase is not consistent for areas in the d01 domain. The greatest increase, both
442 relative and absolute, in the snow depth correlation coefficient occurs in the finer
443 simulation domain in EXP1, where the correlation between observed and modeled
444 snow depth increases by 0.22, which is a 366.7 % increase. The mean and relative
445 increases in the correlation coefficient between observed and modeled snow depth for
446 areas in the d02 simulations are 0.14 and 107.8 %, respectively (Fig. 6b). WRF snow
447 depth estimates are more accurate at finer resolution (i.e., 1 km resolution) than in
448 coarser simulations (i.e., 5 km resolution), regardless of which albedo scheme is
449 implemented (Fig. 6). Implementing the improved albedo scheme in WRF improves
450 the agreement between model estimated and observed snow depth, relative to
451 implementing the default Noah albedo scheme, as seen by the decreased RMSE and the
452 increased correlation coefficient.

453 **3.4 Turbulent heat and vapor fluxes**

454 Albedo plays a significant role in the land surface energy balance. It determines the
455 proportioning of net radiation fluxes between turbulent heat and vapor fluxes. Our study
456 shows that using the improved snow albedo scheme in WRF results in a good model
457 representation of surface albedo in simulations of snow events. We now consider
458 whether replacing the default scheme with the improved scheme may affect the
459 proportioning of net radiation fluxes between turbulent heat and vapor fluxes. Since
460 there are very few observation in situ stations located in the area covered by the finer
461 model domain, a total of 14 in situ stations located in the area covered by d01 were
462 selected, and WRF estimates of turbulent heat and vapor fluxes were assessed from
463 simulations calculated at 5 km resolution (Table 2)

464 The diurnal changes in SH and LH recorded in the in situ observations and calculated

465 in the eight modeling experiments are shown in Figure 7. The WRF model successfully
 466 captures the diurnal changes in SH and LH, particularly in EXP1 and EXP2, where the
 467 model estimates of SH and LH are almost equal to the in situ observations. In the
 468 nighttime, the WRF model accurately estimates SH and LH in all eight experiments.
 469 However, during the day WRF consistently underestimates SH in all experiments
 470 except EXP1 and EXP2, and estimates LH with varying accuracy when the default
 471 Noah albedo scheme is used. For example, when the default Noah scheme is used, WRF
 472 accurately estimates LH in EXP3 and EXP4, but overestimates LH in EXP5 and EXP6
 473 and underestimates LH in EXP7 and EXP8. Compared with WRF estimates calculated
 474 using the default scheme, WRF simulations calculated using the new albedo scheme
 475 result in increased estimates of the turbulent heat and vapor fluxes. This leads to SH
 476 estimates that are closer to observations for experiments EXP3 to EXP8, a greatly
 477 overestimated LH for experiments EXP3 to EXP6, and a slightly overestimated LH,
 478 which is closer to observations for EXP7 and EXP8 (Fig. 7). In general, WRF estimates
 479 of SH are improved through the implementation of the new albedo scheme, relative to
 480 the default scheme, although SH is underestimated during snowfall events. The impact
 481 of the improved albedo scheme on LH estimates varies between the different snowfall
 482 events, but LH is consistently overestimated.

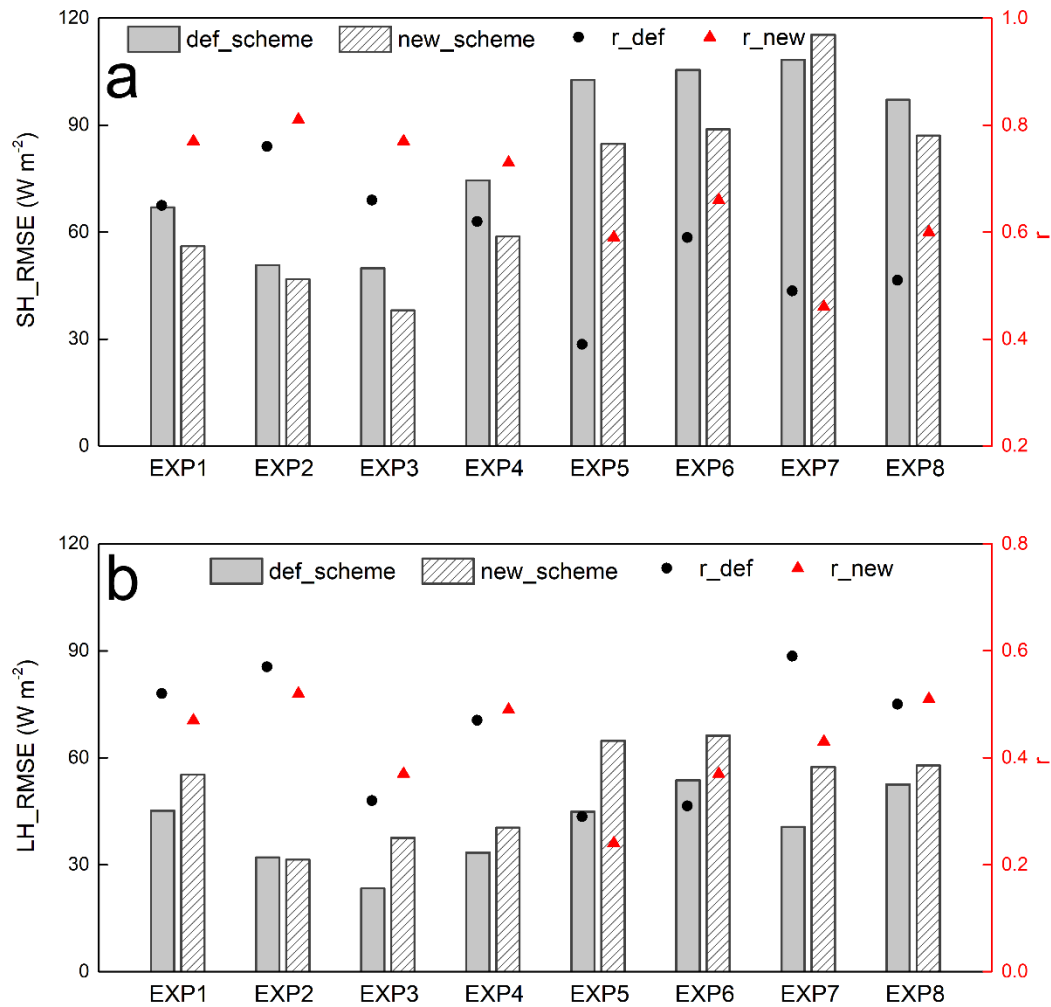


483

484 **Figure 7.** Diurnal change of sensible (SH) and latent (LH) heat fluxes from ground
 485 observations and model estimates. Beginning at 02:00 BST with 3 hours interval. For
 486 def_scheme and new_scheme, see Figure 2.

487 The RMSE and correlation coefficient for comparisons between WRF estimates and
488 observations for SH and LH are shown in Figure 8. Compared with when the default
489 Noah scheme is used, WRF estimates using the improved scheme result in reduced
490 RMSE for SH estimates in all experiments except EXP7. The absolute (and relative)
491 reductions are: 10.9 W m⁻² (16.2 %) in EXP1, 3.9 W m⁻² (7.6 %) in EXP2, 11.9 W m⁻²
492 (23.8 %) in EXP3, 15.7 W m⁻² (21 %) in EXP4, 17.9 W m⁻² (17.4 %) in EXP5, 16.6 W
493 m⁻² (15.8 %) in EXP6, and 10.0 W m⁻² (10.3 %) in EXP8. There is a relative increase
494 of 6.5 % in EXP7. Implementing the improved scheme in WRF significantly increases
495 the correlation coefficients between observed and modeled SH, relative to using the
496 default scheme, in all experiments except EXP7, where there is a slight decrease. The
497 largest increase in the SH correlation coefficient, both absolute and relative, is 0.2 and
498 51.3 %, respectively, and occurs for EXP5. Implementing the improved scheme in WRF
499 reduces the SH RMSE by an average of 10 W m⁻², which is an improvement of 13.2 %
500 improvement, and increases the SH correlation coefficient by an average of 0.1, which
501 is an improvement of 16.8 % (Fig. 8a). However, replacing the default scheme with the
502 improved albedo scheme results in less accurate estimates of LH, and corresponds to
503 an increase in RMSE in almost all eight experiments, although the correlation
504 coefficient increases for half of the snowfall events simulations (EXP3, EXP4, EXP6
505 and EXP8) (Fig. 8b).

506 In summary, the improved snow albedo scheme has a significant effect on the
507 proportioning of radiative fluxes between turbulent heat and vapor fluxes. It
508 significantly outperforms the default Noah scheme in relation to SH estimates, but there
509 is no significant improvement in LH estimates and these may be less accurate when the
510 new scheme is used, relative to the default scheme, during snowfall and the subsequent
511 snowmelt period.



512

513 **Figure 8.** Same as Figure 5, but for sensible (a) and latent (b) heat fluxes. The
 514 correlation coefficient is significant at the 0.001 significance level.

515 **4 Discussion**

516 The highly complex topography of the Tibetan Plateau means that WRF estimates of
 517 air temperature, albedo and snow depth are strongly sensitivity to model resolution. Our
 518 study shows that WRF performs much more accurately when run at finer resolution (1
 519 km) than at relatively coarse resolution (5 km) for snowfall events over the Tibetan
 520 Plateau, regardless of which snow albedo parameterization scheme is used. This
 521 difference may be explained by the ability of the model to resolve complex terrain
 522 (Rahimi et al., 2019), and/or by the implementation of the cumulus convective

523 parameterization scheme. The more detailed representation of complex terrain and the
524 explicit representation of convection mean that running WRF at finer resolution greatly
525 improves model estimates of air temperature, surface pressure, and relative humidity
526 (Singh et al., 2020), and provides small improvements in the magnitude of daytime
527 convective precipitation (Collier and Immerzeel, 2015). Norris et al. (2017) pointed out
528 that decreasing the grid spacing from 6.7 to 2.2 km likely improves estimates of
529 mountain precipitation but does not fundamentally change the representation of the
530 diurnal cycle. They indicated that the key difference between low and high model
531 resolution is whether or not a cumulus convective scheme is required. Subkilometer
532 grid resolution has been investigated in WRF, and used for modeling meteorological
533 variables over complex terrain (Horvath et al., 2012; Dimitrova et al., 2016). The 500
534 m resolution configuration of WRF results in the closest match between the model
535 estimates and observations, and gives the most plausible spatial distribution of
536 precipitation over the complex topography. The performance of the WRF model has
537 been similarly demonstrated to improve at 500 m, relative to coarser resolutions, for
538 wind and air temperature estimates (Bonekamp et al., 2018). We therefore strongly
539 suggest that subkilometer grid resolution should be considered when WRF is
540 configured for simulations covering areas in High Mountain Asia in future research.

541 Our improved snow albedo scheme parameterizes albedo as a function of snow depth
542 and age by considering the relationship between MODIS albedo and the modelled snow
543 depth and age. It is more physically plausible than the default Noah scheme, which
544 considers snow cover, and outperforms the default Noah scheme for air temperature,
545 snow depth, albedo and turbulent heat and vapor fluxes estimates during snowfall
546 events. However, even when the improved albedo scheme is used, the RMSE for WRF
547 estimates of albedo at 5 km spatial resolution remains around 0.21-0.26, although this
548 represents a decrease of 22-45 % relative to when the default albedo scheme is used. It
549 should be noted that the accuracy of the MODIS albedo retrieval algorithm is limited
550 during snowfall events and snowmelt periods (Qin et al., 2011; An et al., 2020), and
551 also that rugged mountain terrain not only affects the radiation absorbed by the land

552 surface, but also affects the radiation reflected by the land surface to the satellite borne
553 sensor. Multiple reflection and scattering from adjacent mountains creates challenges
554 for the monitoring and retrieval of surface albedo in areas of complex terrain via remote
555 sensing (Zhang and Gao, 2011; Roupioz et al., 2014, 2016). This reduces the accuracy
556 of MODIS albedo retrieval over the complex topographic Tibetan Plateau and
557 constitutes a limitation to the improved albedo parameterization investigated here, since
558 it relies on MODIS albedo products. A terrain correction is required for the MODIS
559 albedo retrieval to further improve the albedo parameterization scheme used here.
560 However, it is difficult to establish a unified terrain correction model due to the large
561 undulations of the Tibetan Plateau. How to effectively eliminate the influence of terrain
562 factors from a specific mountain surface on quantitative retrievals from remote sensing
563 data has long been a challenge and a focus for remote sensing research. A further
564 challenge for the assessment presented here is the sparse and uneven distribution of
565 available in situ albedo observation data over the bulk Tibetan Plateau. This paucity of
566 data means that there is a mismatch in spatial resolution when comparing albedo
567 estimates, calculated at 5 km resolution, with in situ observations.

568 Air temperature is a critical factor that is related to albedo and determines energy
569 distribution between SH and LH. Using the improved snow albedo parameterization
570 scheme significantly reduces the albedo overestimates during snowfall events that
571 occur when the default scheme is used, and this leads to the reduction of the cold air
572 temperature bias in the model. Therefore, in this study, the improved scheme reduces
573 the underestimates for SH and improves the performance of WRF for simulating SH
574 over the Tibetan Plateau, relative to when the default scheme is used. These results
575 indicate that the accurate simulation of surface albedo is very important for the accurate
576 simulation of SH.

577 Implementing the improved albedo scheme results in little improvement to estimates of
578 LH calculated, which is restricted by water content and increased only slightly, relative
579 to when the default albedo scheme is used. This may be explained by the LH

580 parameterization scheme used in the Noah LSM (Chen and Dudhia, 2001). The total
581 LH in the Noah LSM has three components (LH from the direct evaporation from the
582 top surface layer, evaporation of precipitation intercepted by the canopy and
583 transpiration via the canopy and roots respectively). The factors affecting calculation
584 of LH in the Noah LSM include not only the radiation balance (which is impacted by
585 albedo), but also soil water, soil capillary conductivity and vegetation status, i.e., albedo,
586 surface heat and water vapor exchange coefficient, saturated water vapor pressure,
587 specific humidity, surface soil water content, field capacity, wilting point, canopy
588 resistance, total precipitation, and canopy interception amount. In our current study, we
589 have focused on the snow albedo parameterization scheme in the Noah LSM by
590 considering the MODIS albedo product and the additional snow related variable of
591 snow depth. Therefore, the influence of our improved scheme on LH estimates
592 calculated by the LSM is very limited.

593 Implementing the improved snow albedo scheme in place of the default scheme greatly
594 decreases the overestimation of albedo from snowmelt to snow free processes, but does
595 not remove the underestimation of albedo during snowfall. This means that the
596 improvements mainly come from snowmelt and snow free simulations, and model
597 performance during snowfall may be worse when the improved albedo scheme is used.
598 This suggests an opportunity to further investigate how albedo is characterized by snow
599 depth and age in the snow albedo parameterization scheme.

600 **5 Conclusions**

601 We conducted several numerical experiments to evaluate the performance of the
602 MODIS albedo based snow albedo parameterization scheme (Liu, 2020) implemented
603 in WRF. We assessed the RMSE and correlation coefficient between observed and
604 modeled air temperature, albedo, snow depth and turbulent heat and vapor fluxes for
605 simulations of eight snowfall events over the Tibetan Plateau. We compared the
606 accuracy of WRF estimates made using the improved snow albedo scheme with that of
607 WRF estimates made using the default Noah scheme, in both cases comparing with

608 ground observations.

609 The accuracy of WRF estimates of albedo is significantly improved when the new
610 albedo scheme is implemented. The default Noah scheme tends towards higher albedo
611 estimates and cannot accurately capture snowfall and snowmelt processes, resulting in
612 a high RMSE and low correlation coefficient between modeled and observed albedo.
613 Through consideration of snow related variables, such as snow depth and age, and by
614 being based on MODIS remote sensing albedo products, the improved scheme
615 estimates albedo more accurately than the default scheme, improving the albedo RMSE
616 by around 22 % to 45 %, with an average improvement of 32 %. Similarly, the improved
617 scheme results in an increased correlation coefficient between modeled and observed
618 albedo. Relative to the default scheme, the correlation coefficient relatively increases
619 by around 16 % to 151 %, with an average improvement of 69 %. This may contribute
620 to the relatively better performance of WRF for simulating air temperatures when the
621 improved albedo scheme is used. The improved scheme relatively decreases (increases)
622 the air temperature RMSE (correlation coefficient) by 16 % (1.5 %) for model estimates
623 calculated at 5 km resolution, and by 27 % (5 %) for model estimates calculated at 1
624 km resolution.

625 There are mutual feedbacks between snow and albedo. During snowfall and over the
626 subsequent snowmelt period, snow depth and age affect changes in the albedo. The
627 changes in albedo in turn affect the evolution of snow events by changing the surface
628 energy budget and the proportional distribution of net radiation between turbulent heat
629 and vapor fluxes, and finally by changing the type of precipitation. Our study shows
630 that when the default albedo scheme is replaced by the improved albedo scheme in
631 WRF, the turbulent heat and vapor fluxes estimates increase. The improved scheme
632 significantly outperforms the default Noah scheme for SH estimates, with a reduction
633 (increase) in the RMSE (correlation coefficient) of 10 W m^{-2} (0.1), representing an
634 improvement of 13 % (17 %). The overall accuracy with which WRF estimates
635 turbulent heat and vapor fluxes improves when the improved albedo scheme replaces

636 the default scheme, although there is no significant improvement in LH estimates. This
637 overall improvement leads to a more accurate reproduction of the evolution of snowfall
638 events and to more accurate snow depth estimates. Our study shows that using the
639 improved albedo scheme in WRF reduces the RMSE and increases the correlation
640 coefficient between modeled and observed snow depth, relative to using the default
641 scheme. This improvement is more significant for simulations at 1 km resolution than
642 for simulations at 5 km resolution, with maximum and averaged relative RMSE
643 (correlation coefficient) decreases (increases) of 42 % (367 %) and 21 % (108 %),
644 respectively for 1 km resolution simulations.

645 **Acknowledgements**

646 This research was supported by the Strategic Priority Research Program of Chinese
647 Academy of Sciences (XDA20060101), the Second Tibetan Plateau Scientific
648 Expedition and Research program (STEP) (2019QZKK0103), the National Natural
649 Science Foundation of China (41661144043, 91637312, 41830650, 91737205), MOST
650 High Level Talent grant No. G20190161018, the Chinese Academy of Sciences
651 President's International Fellowship Initiative Grant No. 2020VTA0001, the Key
652 Research Program of Frontier Sciences of Chinese Academy of Sciences (QYZDJ-
653 SSW-DQC019) and Key Research and Development Projects of the Ministry of
654 Science and Technology (2018YFC1505701). The authors express thanks to ECMWF
655 for sharing atmospheric reanalysis data set (ERA5 dataset is available from
656 <https://www.ecmwf.int/en/forecasts/datasets/reanalysis-datasets/era5>), to NASA for
657 offering MODIS reflectance products (<https://modis.gsfc.nasa.gov/>), and to staff from
658 CMA, CAS and Qilian Mountains integrated observatory network for very hard work
659 in meteorological observations and offering the data (CMA meteorological data is
660 available from <http://data.cma.cn/en>; albedo and turbulent heat and vapor fluxes
661 observations from CAS and Qilian Mountains integrated observatory network is
662 provided by National Tibetan Plateau Data Center (<http://data.tpdac.ac.cn>). The first
663 author would like to acknowledge all group members for their help in completing this

664 paper.

665 **Reference**

666 An, Y., Meng, X., Zhao, L., Li, Z., Wang, S., Shang, L., Chen, H., Lyu, S., Li, G., and
667 Ma, Y.: Performance of GLASS and MODIS satellite albedo products in diagnosing
668 albedo variations during different time scales and special weather conditions in the
669 Tibetan Plateau, *Remote Sens.*, 12, 2456, 2020.

670 Aoki, T., Hachikubo, A., and Hori, M.: Effects of snow physical parameters on
671 shortwave broadband albedos, *J. Geophys. Res.*, 108, D19, 2003.

672 Bao, Y. and Lyu, S.: Improvement of surface albedo parameterization within a regional
673 climate model (regcm3), *Hydrol. Earth Syst. Sci.*, 6, 1651-1676, 2009.

674 Bao, Y., Lyu, S., Zhang, Y., Meng, X., and Yang, S.: Improvement of surface albedo
675 simulations over arid regions, *Adv. Atmos. Sci.*, 25, 481-488, 2008.

676 Bloch, M. R.: Dust-induced albedo changes of polar ice sheets and glacierization, *J.*
677 *Glaciol.*, 5, 241-244, 1964.

678 Bonekamp, P. N. J., Collier, E., and Immerzeel, W. W.: The impact of spatial resolution,
679 land use, and spinup time on resolving spatial precipitation patterns in the Himalayas,
680 *J. Hydrometeorol.*, 19, 1565-1581, 2018.

681 Chen, F. and Dudhis, J.: Coupling an advanced land surface-hydrology model with the
682 Penn State-NCAR MM5 modeling system. Part I: Model implementation and
683 sensitivity, *Mon. Weather Rev.*, 129, 569-585, 2001.

684 Collier, E. and Immerzeel, W. W.: High-resolution modeling of atmospheric dynamics
685 in the Nepalese Himalaya, *J. Geophys. Res.*, 120, 9882-9896, 2015.

686 Dang, C., Brandt, R. E., and Warren, S. G.: Parameterizations for narrowband and
687 broadband albedo of pure snow and snow containing mineral dust and black carbon, *J.*

688 Geophys. Res., 120, 5446-5468, 2015.

689 Dimitrova, R., Silver, Z., Zsedrovits, T., Hocut, C. M., Leo, L. S., Di Sabatino, S., and
690 Fernando, H. J. S.: Assessment of planetary boundary-layer schemes in the Weather
691 Research and Forecasting mesoscale model using Materhorn field data, Bound-Lay
692 Meteorol., 159, 589-609, 2016.

693 Ek, M. B., Mitchell, K. E., Lin, Y., Rogers, E., Grunmann, P., Koren, V., Gayno, G., and
694 Tarpley, J. D.: Implementation of Noah land surface model advances in the National
695 Centers for Environmental Prediction operational mesoscale Eta model, J. Geophys.
696 Res., 108, D22, 2003.

697 Gao, Y., Xu, J., and Chen, D.: Evaluation of WRF mesoscale climate simulations over
698 the Tibetan Plateau during 1979-2011, J. Clim., 28, 2823-2841, 2015.

699 Gardner, A. S. and Sharp, M. J.: A review of snow and ice albedo and the development
700 of a new physically based broadband albedo parameterization, J. Geophys. Res., 115,
701 F1, 2010.

702 Hansen, J. and Nazarenko, L.: Soot climate forcing via snow and ice albedos, PNAS,
703 101, 423-428, 2004.

704 He, C., Takano, Y., Liou, K.-N., Yang, P., Li, Q., and Chen, F.: Impact of snow grain
705 shape and black carbon-snow internal mixing on snow optical properties:
706 Parameterizations for climate models, J. Clim., 30, 10019-10036, 2017.

707 He, C., Liou, K.-N., and Takano, Y.: Resolving size distribution of black carbon
708 internally mixed with snow: Impact on snow optical properties and albedo, Geophys.
709 Res. Lett., 45, 2697-2705, 2018a.

710 He, C., Liou, K.-N., Takano, Y., Yang, P., Qi, L., and Chen, F.: Impact of grain shape
711 and multiple black carbon internal mixing on snow albedo: Parameterization and
712 radiative effect analysis, J. Geophys. Res., 123, 1253-1268, 2018b.

713 Horvath, K., Koracin, D., Vellore, R., Jiang, J., and Belu, R.: Sub-kilometer dynamical
714 downscaling of near-surface winds in complex terrain using WRF and MM5 mesoscale
715 models, *J. Geophys. Res.*, 117, D11, 2012.

716 Jonsell, U., Hock, R., and Holmgren, B.: Spatial and temporal variations in albedo on
717 Storglaciaren, Sweden, *J. Glaciol.*, 49, 59-68, 2003.

718 Kuipers Munneke, P., van den Broeke, M. R., Lenaerts, J. T. M., Flanner, M. G.,
719 Gardner, A. S., and van de Berg, W. J.: A new albedo parameterization for use in climate
720 models over the Antarctic ice sheet, *J. Geophys. Res.*, 116, D5, 2011.

721 Li, X.: Qilian Mountains integrated observatory network: Dataset of Qinghai Lake
722 integrated observatory network (eddy covariance system of Alpine meadow and
723 grassland ecosystem Superstation, 2018), National Tibetan Plateau Data Center, 2019.

724 Li, Y. and Hu, Z.: A study on parameterization of surface albedo over grassland surface
725 in the northern Tibetan Plateau, *Adv. Atmos. Sci.*, 26, 161-168, 2009.

726 Liang, S.: Narrowband to Broadband conversions of land surface albedo: I. Algorithms,
727 *Remote Sens. Environ.*, 76, 213-238, 2000.

728 Liang, X., Xu, M., Gao, W., Kunkel, K., Slusser, J., Dai, Y., Min, Q., Houser, P. R.,
729 Rodell, M., Schaaf, C. B., and Gao, F.: Development of land surface albedo
730 parameterization based on Moderate Resolution Imaging Spectroradiometer (MODIS)
731 data, *J. Geophys. Res.*, 110, D11, 2005.

732 Lin, P., Wei, J., Yang, Z., Zhang, Y., and Zhang, K.: Snow data assimilation-constrained
733 land initialization improves seasonal temperature prediction, *Geophys. Res. Lett.*, 43,
734 11423-11432, 2016.

735 Liu, L.: Diagnostic analysis and numerical simulation of a regional heavy snowfall over
736 the Tibetan Plateau, Doctoral dissertation, Chapter 5, Institute of Tibetan Plateau
737 Research, Chinese Academy of Sciences, Building 3, Courtyard 16, Lincui Road,

738 Chaoyang District, Beijing, China, 2020.

739 Liu, L., Ma, Y., Menenti, M., Zhang, X., and Ma, W.: Evaluation of WRF modeling in
740 relation to different land surface schemes and initial and boundary conditions: A snow
741 event simulation over the Tibetan Plateau, *J. Geophys. Res.*, 124, 209-226, 2019.

742 Liu, S., Che, T., Xu, Z., Ren, Z., Tan, J., and Zhang, Y.: Qilian Mountains integrated
743 observatory network: Dataset of Heihe integrated observatory network (Large aperture
744 scintillometer of Daman Superstation, 2019), National Tibetan Plateau Data Center,
745 2020.

746 Livneh, B., Xia, Y., Mitchell, K. E., Ek, M. B., and Lettenmaier, D. P.: Noah LSM snow
747 model diagnostics and enhancements, *J. Hydrometeorol.*, 11, 721-738, 2010.

748 Ma, Y., Wang, Y., and Han, C.: Regionalization of land surface heat fluxes over the
749 heterogeneous landscape: from the Tibetan Plateau to the Third Pole region, *Int. J.*
750 *Remote Sens.*, 39, 5872-5890, 2018.

751 Ma, Y., Hu, Z., Xie, Z., Ma, W., Wang, B., Chen, X., Li, M., Zhong, L., Sun, F., Gu, L.,
752 Han, C., Zhang, L., Liu, X., Ding, Z., Sun, G., Wang, S., Wang, Y., and Wang, Z.: A
753 long-term (2005-2016) dataset of hourly integrated land-atmosphere interaction
754 observations on the Tibetan Plateau, *Earth Syst. Sci. Data*, 12, 2937-2957, 2020.

755 Malik, M. J., van der Velde, R., Vekerdy, Z., and Su, Z.: Improving modeled snow
756 albedo estimates during the spring melt season, *J. Geophys. Res.*, 119, 7311-7331, 2014.

757 Maussion, F., Scherer, D., Finkelnburg, R., Richters, J., Yang, W., and Yao, T.: WRF
758 simulation of a precipitation event over the Tibetan Plateau, China-an assessment using
759 remote sensing and ground observations, *Hydrol. Earth Syst. Sci.*, 15, 1795-1817, 2011.

760 Meng, C. and Li, H.: Solar radiation partitioning and surface albedo parameterization
761 in the hinterland of Taklimakan Desert, *Adv. Meteorol.*, 1-8, 2019.

762 Meng, X., Lyu, S., Zhang, T., Zhao, L., Li, Z., Han, B., Li, S., Ma, D., Chen, H., Ao, Y.,

763 Luo, S., Shen, Y., Guo, J., and Wen, L.: Simulated cold bias being improved by using
764 MODIS time-varying albedo in the Tibetan Plateau in WRF model, *Environ. Res. Lett.*,
765 13, 44028, 2018.

766 Norris, J., Carvalho, L. M. V., Jones, C., Cannon, F., Bookhagen, B., Palazzi, E., and
767 Tahir, A. A.: The spatiotemporal variability of precipitation over the Himalaya:
768 Evaluation of one-year WRF model simulation, *Clim. Dynam.*, 49, 2179-2204, 2017.

769 Oerlemans, J. and Knap, W. H.: A 1 year record of global radiation and albedo in the
770 ablation zone of Morteratschgletscher, Switzerland, *J. Glaciol.*, 44, 231-238, 1998.

771 Park, S. and Park, S. K.: Parameterization of the snow-covered surface albedo in the
772 Noah-MP version 1.0 by implementing vegetation effects, *Geosci. Model Dev.*, 9, 1073-
773 1085, 2016.

774 Qin, J., Yang, K., Liang, S., Zhang, H., Ma, Y., Guo, X., and Chen, Z.: Evaluation of
775 surface albedo from GEWEX-SRB and ISCCP-FD data against validated MODIS
776 product over the Tibetan Plateau, *J. Geophys. Res.*, 116, D24, 2011.

777 Rahimi, S. R., Wu, C., Liu, X., and Brown, H.: Exploring a variable-resolution
778 approach for simulating regional climate over the Tibetan Plateau using VR-CESM, *J.*
779 *Geophys. Res.*, 124, 4490-4513, 2019.

780 Rai, A., Saha, S. K., and Sujith, K.: Implementation of snow albedo schemes of varying
781 complexity and their performances in offline Noah and Noah coupled with NCEP
782 CFSv2, *Clim. Dynam.*, 53, 1261-1276, 2019.

783 Roupioz, L., Nerry, F., Jia, L., and Menenti, M.: Improved surface reflectance from
784 remote sensing data with sub-pixel topographic information, *Remote Sens.*, 6, 10356-
785 10374, 2014.

786 Roupioz, L., Jia, L., Nerry, F., and Menenti, M.: Estimation of daily solar radiation
787 budget at kilometer resolution over the Tibetan Plateau by integrating MODIS data

788 products and a DEM, *Remote Sens.*, 8, 2016.

789 Saito, M., Yang, P., Loeb, N. G., and Kato, S.: A novel parameterization of snow albedo
790 based on a two-layer snow model with a mixture of grain habits, *J. Atmos. Sci.*, 76,
791 1419-1436, 2019.

792 Sellers, P. J., Randall, D. A., Collatz, G. J., Berry, J. A., Field, C. B., Dazlich, D. A.,
793 Zhang, C., Collelo, G. D., and Bounoua, L.: A revised land surface parameterization
794 (SiB2) for atmospheric GCMs. Part I: Model formulation, *J. Clim.*, 9, 676-705, 1996.

795 Skamarock, W., Klemp, J. B., Dudhia, J., Gill, D. O., Barker, D. M., Wang, W., and
796 Powers, J. G.: A description of the advanced research WRF version 3, NCAR Technical
797 Note NCAR/TN-475+STR, 2008.

798 Singh, J., Singh, N., Ojha, N., Sharma, A., Pozzer, A., Kiran Kumar, N., Rajeev, K.,
799 Gunthe, S. S., and Kotamarthi, V. R.: Effects of spatial resolution on WRF v3.8.1
800 simulated meteorology over the central Himalaya, *Geosci. Model Dev.*, 2020.

801 Wang, J., Cui, Y., He, X., Zhang, J., and Yan, S.: Surface albedo variation and its
802 influencing factors over Dongkemadi glacier, central Tibetan Plateau, *Adv. Meteorol.*,
803 852098, 2015.

804 Wang, W., Yang, K., Zhao, L., Zheng, Z., Lu, H., Mamtimin, A., Ding, B., Li, X., Zhao,
805 L., Li, H., Che, T., and Moore, J. C.: Characterizing surface albedo of shallow fresh
806 snow and its importance for snow ablation on the interior of the Tibetan Plateau, *J.*
807 *Hydrometeorol.*, 21, 815-827, 2020.

808 Wang, Z., Zeng, X., and Barlage, M.: Moderate Resolution Imaging Spectroradiometer
809 bidirectional reflectance distribution function-based albedo parameterization for
810 weather and climate models, *J. Geophys. Res.*, 112, 2007.

811 Warren, S. G. and Wiscombe, W. J.: A model for the spectral albedo of snow .II: Snow
812 containing atmospheric aerosols, *J. Atmos. Sci.*, 37, 2734-2745, 1980.

813 Wen, J., Su, Z., Tian, H., Shi, X., Zhang, Y., Wang, X., Liu, R., Zhang, T., Kang, Y.,
814 Lyu, S., and Zhang, J.: Advances in observation and modeling of land surface processes
815 over the source region of the Yellow River, *Advances in Earth Science*, 26, 575-585,
816 2011.

817 Wiscombe, W. J. and Warren, S. G.: A model for the spectral albedo of snow. I: Pure
818 snow, *J. Atmos. Sci.*, 37, 2712-2733, 1980.

819 Xu, J. and Shu, H.: Assimilating MODIS-based albedo and snow cover fraction into the
820 common land model to improve snow depth simulation with direct insertion and
821 deterministic ensemble Kalman filter method, *J. Geophys. Res.*, 119, 10684-10701,
822 2014.

823 Xue, Y., Houser, P. R., Maggioni, V., Mei, Y. W., Kumar, S. V., and Yoon, Y.:
824 Assimilation of satellite-based snow cover and freeze/thaw observations over high
825 mountain Asia, *Front. Earth Sci.*, 7, 2019.

826 Yuan, W., Xu, W., Ma, M., Chen, S., Liu, W., and Cui, L.: Improved snow cover model
827 in terrestrial ecosystem models over the Qinghai-Tibetan Plateau, *Agr. For. Meteorol.*,
828 218, 161-170, 2016.

829 Zhang, W. and Gao, Y.: Topographic correction algorithm for remotely sensed data
830 accounting for indirect irradiance, *Int. J. Remote Sens.*, 32, 1807-1824, 2011.

831 Zhang, Y., Hoar, T. J., Yang, Z., Anderson, J. L., Toure, A. M., and Rodell, M.:
832 Assimilation of MODIS snow cover through the data assimilation research testbed and
833 the community land model version 4, *J. Geophys. Res.*, 119, 7091-7103, 2014.

834 Zhao, C. and Zhang, R.: Cold and Arid Research Network of Lanzhou university (eddy
835 covariance system of Guazhou station, 2019), National Tibetan Plateau Data Center,
836 2020.

837 Zhong, E., Li, Q., Sun, S., Chen, W., Chen, S., and Nath, D.: Improvement of a snow

838 albedo parameterization in the snow–atmosphere–soil transfer model: Evaluation of
839 impacts of aerosol on seasonal snow cover, *Adv. Atmos. Sci.*, 34, 1333-1345, 2017.